

Flexible Gravitational-Wave Parameter Estimation with Transformers

Annalena Kofler,^{1, 2, *} Maximilian Dax,^{1, 3, 4} Stephen R. Green,⁵ Jonas Wildberger,³ Nihar Gupte,^{2, 6} Jakob H. Macke,^{1, 7} Jonathan Gair,² Alessandra Buonanno,^{2, 6} and Bernhard Schölkopf^{1, 3}

¹ Max Planck Institute for Intelligent Systems, Max-Planck-Ring 4, 72076 Tübingen, Germany

² Max Planck Institute for Gravitational Physics (Albert Einstein Institute), Am Mühlenberg 1, 14476 Potsdam, Germany

³ ELLIS Institute Tübingen, Maria-von-Linden-Straße 2, 72076 Tübingen, Germany

⁴ Tübingen AI Center, Maria-von-Linden-Straße 1, 72076 Tübingen, Germany

⁵ Nottingham Centre of Gravity & School of Mathematical Sciences, University of Nottingham, University Park, Nottingham, NG7 2RD, United Kingdom

⁶ Department of Physics, University of Maryland, College Park, MD 20742, USA

⁷ Machine Learning in Science, University of Tübingen & Tübingen AI Center, 72076 Tübingen, Germany

Gravitational-wave data analysis relies on accurate and efficient methods to extract physical information from noisy detector signals, yet the increasing rate and complexity of observations represent a growing challenge. Deep learning provides a powerful alternative to traditional inference, but existing neural models typically lack the flexibility to handle variations in data analysis settings. Such variations accommodate imperfect observations or are required for specialized tests, and could include changes in detector configurations, overall frequency ranges, or localized cuts. We introduce a flexible transformer-based architecture paired with a training strategy that enables adaptation to diverse analysis settings at inference time. Applied to parameter estimation, we demonstrate that a *single* flexible model—called DINGO-T1—can (i) analyze 48 gravitational-wave events from the third LIGO-Virgo-KAGRA Observing Run under a wide range of analysis configurations, (ii) enable systematic studies of how detector and frequency configurations impact inferred posteriors, and (iii) perform inspiral-merger-ringdown consistency tests probing general relativity. DINGO-T1 also improves median sample efficiency on real events from a baseline of 1.4% to 4.2%. Our approach thus demonstrates flexible and scalable inference with a principled framework for handling missing or incomplete data—key capabilities for current and next-generation observatories.

Introduction.—Gravitational waves (GWs) provide unique access to the strong-field dynamics of compact objects and have transformed our ability to probe astrophysics, cosmology, and fundamental physics [1–8]. Drawing scientific conclusions from GW observations requires accurate and efficient data analysis, yet conventional Bayesian techniques [9, 10] are computationally expensive and difficult to scale to the growing volume and complexity of data. Machine learning offers a promising solution by leveraging neural networks to process strain data and predict physical quantities, and has seen applications to detection [11–13], noise classification [14], source localization [15, 16], and parameter estimation (PE) [17–27]. For PE, neural simulation-based inference (SBI, [28]) has reduced analysis times to the order of a few seconds—crucial for handling increased event rates [29, 30] and enabling rapid multi-messenger follow-up [1].

This speed-up arises from front-loading computational costs: once trained on millions of simulated data sets, neural networks can analyze new observations at negligible expense. However, conventional neural architectures operate on a fixed input dimension, requiring the data representation to be fixed prior to training. A trained model is therefore tied to specific detector combinations and data-conditioning settings—a major barrier to widespread adoption. Existing models cannot readily adapt to detectors being offline, to restricted frequency bands used to mitigate noise contamination, or to data gaps expected in LISA observations [31].

In this *Letter*, we propose a neural architecture and training strategy that enable flexible analysis of heterogeneous GW data. The key idea is to process strain data using a transformer encoder and exploit its ability to handle input sequences of arbitrary length [32]. We partition data sets into sequences of short strain segments called tokens, and randomly drop tokens during training to mimic frequency cuts and missing detectors. Through the self-attention mechanism, the model learns to identify correlations between strain segments, capturing global dependencies across detectors and frequencies, and to marginalize over missing data. Although transformers have been used for a range of GW tasks [33–39], previous work has not leveraged their inherent flexibility in handling variable-length or incomplete data. Our approach is inspired by works on missing data in SBI [40–43].

We integrate the transformer encoder into the DINGO framework for GW PE, yielding a flexible model that we call DINGO-T1 (DINGO Transformer, version 1; see Fig. 1). We demonstrate its versatility and performance through injection studies and analyses of real data. In particular, we reanalyze 48 events from the LIGO-Virgo-KAGRA (LVK) [44–46] third observing run (O3) [29, 30, 47, 48], spanning 17 combinations of detectors and frequency ranges, with a single network. Compared to baseline neural posterior estimation (NPE) networks with residual network encoders [22], DINGO-T1 improves median importance sampling efficiency from 1.4% to 4.2%. We further analyze all events using all possible LIGO-Virgo

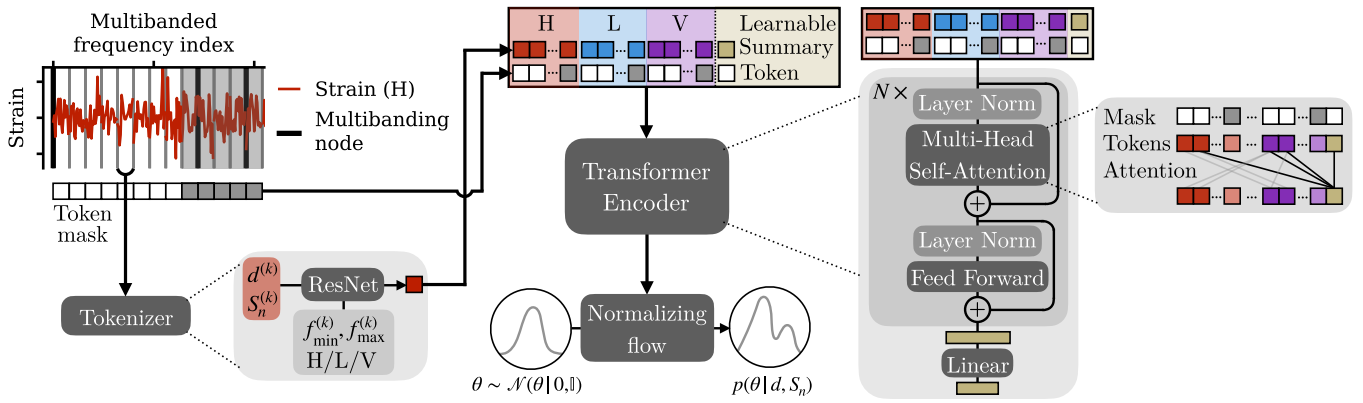


Figure 1. Overview of DINGO-T1. After multibanding, data and detector PSD segments ($d^{(k)}, S_n^{(k)}$) are mapped by a shared tokenizer into tokens that also encode the frequency range ($f^{(k)}, f^{(k+1)}$) and detector identity I . The sequence of tokens is masked, augmented with a learnable summary token, and processed by the transformer encoder. Through self-attention, the summary token aggregates information from all unmasked segments. The final summary token is projected via a linear layer to a 128-dimensional feature vector, which conditions a normalizing flow to model the posterior $p(\theta|d, S_n)$.

detector combinations. Such studies are extremely costly for standard methods, but can be used to identify data systematics. As a final demonstration, we use frequency cuts to perform inspiral-merger-ringdown consistency tests on seven events. Previously, conducting all of these experiments would have required training 94 different models to handle the disparate settings.

Our study thus represents a step towards generalized inference models in GW astronomy, enabling flexible choice of detector and frequency settings without retraining. This flexibility opens new prospects for analyzing large catalogs [29, 30], facilitating rapid assessments of systematics and consistency across diverse data-analysis settings [49, 50], as well as more robust approaches to missing data. In addition, our transformer model DINGO-T1¹ serves as a powerful and general encoder for GW data which could be fine-tuned on other tasks such as GW detection, providing a foundation for efficient and scalable GW science.

Architecture.—For NPE [53–55], one trains a neural network $q(\theta|d)$ to estimate the Bayesian posterior $p(\theta|d)$ over parameters θ given data d . In the context of GW single-event inference, θ denotes the source parameters, e.g., of a black hole binary, and d denotes the strain data measured at the detectors [56]. For DINGO, we also augment the strain data with an estimate of the noise power spectral density (PSD), which varies from event to event [22]. Data are generally of high dimension ($\gg 10^4$), so d is first mapped by an embedding network f_ϕ to a lower-dimensional representation. This compressed summary is then passed to a density estimator \hat{q}_φ to

model the posterior, $q(\theta|d) = \hat{q}_\varphi(\theta|f_\phi(d))$. The learnable parameters $\{\phi, \varphi\}$ are optimized jointly during training.

Our core architectural change is to replace the traditional embedding network with a transformer encoder (Fig. 1), which naturally handles sequences of variable length. We divide the strain data sets into small segments, which a tokenizer network maps to token embeddings (Fig. 1 left). These embeddings form a sequence that the transformer encoder processes. We now describe the tokenization scheme, model architecture, and training strategy; full technical details appear in the Supplemental Material.

We represent GW data $d = \{d_I\}_{I=H,L,V}$ as frequency series from the Hanford (H), Livingston (L), and Virgo (V) detectors. We use a multi-banded (non-uniform) frequency grid, with coarser resolution at higher frequencies, designed to capture the chirping morphology of GW signals, and achieve an initial compression of the data [26, 57, 58]. To tokenize, we partition the grid into K equal-length segments with boundary nodes $(f^{(k)})_{k=0}^{K+1}$, such that each interval $(f^{(k)}, f^{(k+1)})$ has a uniform frequency grid (Fig. 1, vertical gray lines). The data d_I and PSD $S_{n,I}$ are processed identically for each detector, yielding $3K$ segments $(d_I^{(k)}, S_{n,I}^{(k)})$, each containing 16 frequency bins.

Each data segment is converted into a token embedding $t(d_I^{(k)}, S_{n,I}^{(k)}, f^{(k)}, f^{(k+1)}, I)$ by a shared tokenizer network t (see Fig. 1, bottom left). Transformer-based architectures are invariant under token permutations, so conditioning tokens on frequency range and detector identity is necessary for interpreting each segment [59]. Finally, we append one additional learnable summary token to the sequence so that the model has a dedicated place to store relevant information extracted across tokens [60, 61].

The full token sequence is passed to a transformer en-

¹ Weights for DINGO-T1 and DINGO baseline [51], as well as corresponding code are publicly available: <https://github.com/dingo-gw/dingo-T1>. The model was trained taking [52] into account.

coder [32, 62, 63], which extracts information relevant for parameter estimation. After the final transformer layer, we compress the summary token to a 128-dimensional feature vector, which conditions a normalizing flow with a rational-quadratic spline coupling transform [64], using the same hyperparameters as in [23].

Training.—We train the DINGO-T1 model—the tokenizer, transformer encoder, and normalizing flow—end-to-end using a negative log likelihood loss. To enable inference under missing data, we mask tokens randomly during training [65]. This has the effect of dropping segments of data, so that the network learns to interpret inputs with missing data. By applying a token mask m to (d, S_n) , our loss takes the form

$$\mathcal{L} = \mathbb{E}_{p(\theta)p(S_n)p(d|\theta, S_n)p(m)} [-\log q(\theta|m(d), m(S_n))], \quad (1)$$

where $p(m)$ denotes the probability of sampling mask m .

We employ a data-based approach to masking, i.e., we choose $p(m)$ to reflect realistic variations in data analysis settings. This includes dropping all tokens corresponding to certain detectors, removing tokens to update minimum and maximum frequencies, and applying random cuts within the frequency range. We also compare to a masking strategy where tokens are dropped uniformly at random, but find that the data-based approach gives better performance. (See the Supplemental Material for complete details on masking.)

We train on simulated data consisting of waveforms generated from the IMRPhenomXPHM model [66] with additive stationary Gaussian noise. Our dataset includes $2.5 \cdot 10^7$ intrinsic waveforms, with extrinsic parameters generated on-the-fly during training. Priors are the same as [23], except for the luminosity distance, which we take as uniform over the range $[0.1, 6]$ Gpc; we infer all parameters except for the phase, which is reconstructed in post-processing [22]. We generate noise during training based on a collection of Welch PSDs estimated across O3 [22]. Models are trained on 8 NVIDIA-A100 GPUs using distributed data parallelization [67, 68] which takes approximately 9.5 days (183 epochs) for DINGO-T1.

At inference time, we only include tokens corresponding to available data that we wish to analyze, omitting those associated with missing information (e.g., a non-observing detector or masked frequency ranges). To validate and correct the resulting posterior, we apply importance sampling (IS) [23], reweighting samples from $q(\theta|d, S_n)$ to the exact posterior defined by the ranges of the original uniform-frequency data. Due to variance in the distribution of importance weights, the effective number of weighted samples is smaller than the number of unweighted samples. This ratio (the sample efficiency) serves as a performance metric.

Results.—We first evaluate DINGO-T1 on 1000 simulated GW signals for each subset of the three detectors HLV, with injections performed over the full frequency

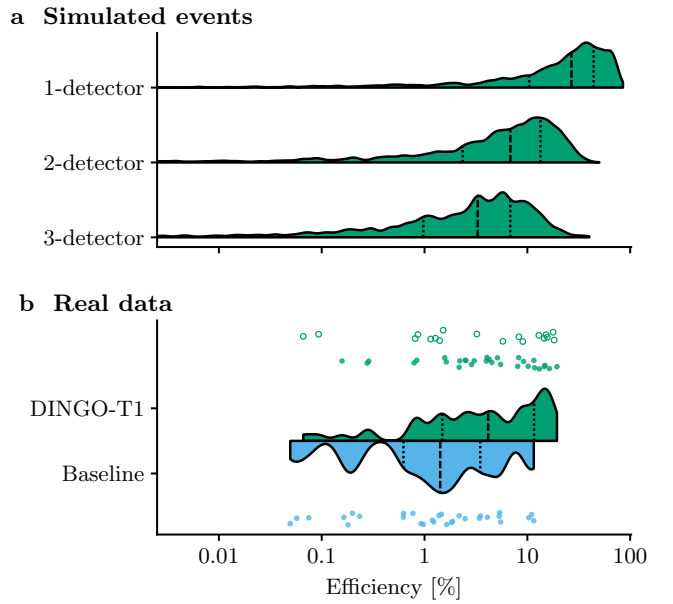


Figure 2. (a) Sample efficiency distribution of 1000 simulated events per detector configuration for the DINGO-T1 model, shown as violin plots. (b) Sample efficiency distribution of DINGO-T1 and the DINGO baseline across 48 real GW events. Dots denote 3-detector events, while circles refer to 2-detector events which cannot be analyzed with the unflexible DINGO baseline. The dashed line represents the median, the dotted lines the quartiles. The efficiencies between simulated (a) and real data (b) are not directly comparable since the parameters are drawn from different distributions.

range. For each injection, we generate 10^5 posterior samples and perform IS. Initial sampling takes under five seconds, with phase reconstruction and IS requiring an additional five to ten minutes on 64 CPU cores. Median efficiencies are 26.9%, 6.8%, and 3.3% for one-, two-, and three-detector configurations, respectively (Fig. 2a). Efficiencies decrease as more detectors are included, consistent with expectations: posteriors constrained by more detectors are narrower and therefore more challenging to learn for normalizing flows. To show that DINGO-T1 is well calibrated, we provide P-P plots for each detector configuration and additional information in the Supplemental Material.

Second, we evaluate DINGO-T1 on all events from O3 that fall within our prior, employing the specific data analysis settings from the official catalogs [29, 30]. For each event, we obtain posterior samples as above and summarize sample efficiencies in Fig. 2b. Across the 48 events, we find a median efficiency of 4.2%; 2-detector events perform slightly better at 4.5%, while 3-detector events reach 4.2%. This outperforms a baseline DINGO NPE model trained for fixed data analysis settings, which obtains a median efficiency of 1.4% across 30 HLV events evaluated on the full frequency range. In general, sample efficiencies of real data (in contrast to injections) can be

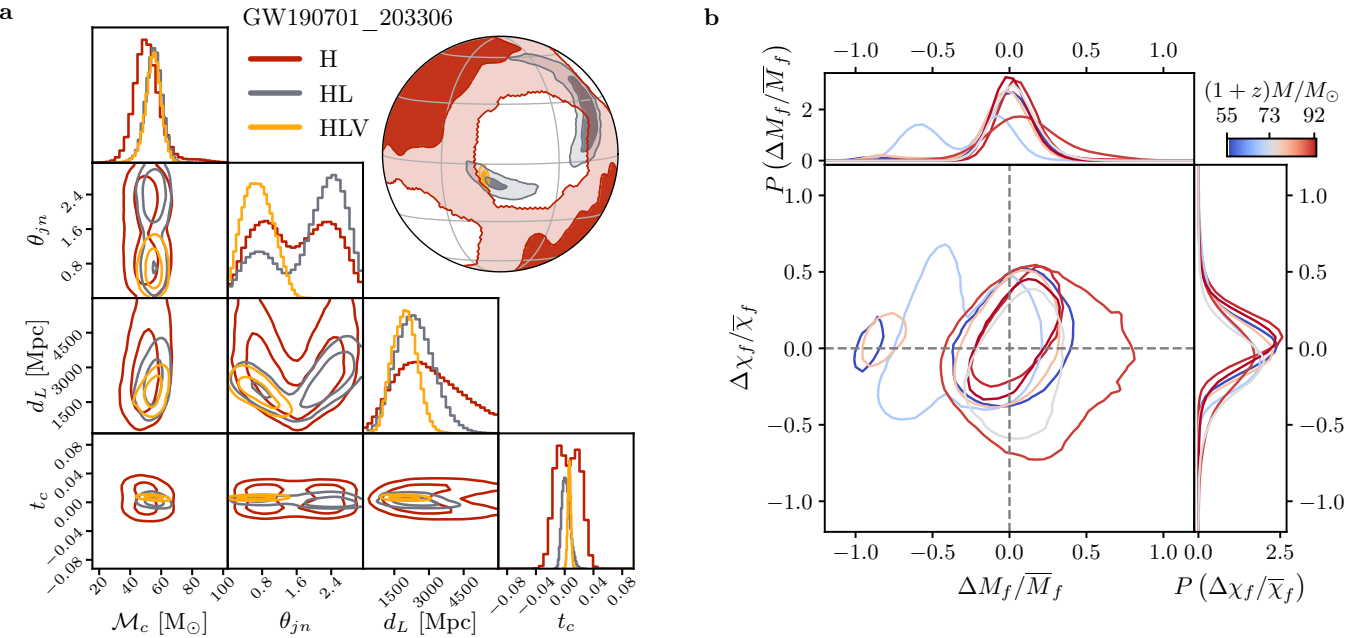


Figure 3. (a) Posterior distribution for GW190701_203306, showing DINGO-T1 analyses for three different detector configurations. (b) Inspiral-merger-ringdown consistency tests for seven events where the signal was analyzed with the DINGO-T1 model on the inspiral and postinspiral part of the signal. The main panel shows the 90% credible regions of the 2D posteriors on $(\Delta M_f / \bar{M}_f, \Delta \chi_f / \bar{\chi}_f)$ and the side panels show the marginalized posteriors. The color corresponds to the median redshifted total mass obtained from posterior samples of the full signal.

negatively impacted by misspecification of the signal and noise model.

It should be noted that our results are not directly comparable to past work [23] by some of us, which reported $\sim 10\%$ median efficiency on O3 events. That study performed HL analyses only; when restricting to HL detectors we find 11% median efficiency with DINGO-T1 (see Supplemental Material). Ref. [23] also incorrectly accounted for the window factor in the likelihood, likely resulting in lower efficiencies [52]. More importantly, Ref. [23] used *group-equivariant* NPE (GNPE, [22, 69]), an algorithm which simplifies data representations by iteratively aligning merger times in each detector. GNPE improves accuracy, but results in substantially longer analysis times as it breaks access to the probability density. DINGO-T1 is based on standard NPE, making inference faster and simpler.

Applications.—To explore the impact of detector configuration on the posterior, we evaluate every event on all possible combinations. While such studies are computationally infeasible with standard samplers, total inference times of under ten minutes per event make it a reasonable analysis with DINGO-T1. We illustrate the effect on the posterior distribution for an example event in Fig. 3a. (See Supplemental Material for detailed discussions.)

Finally, we utilize the flexibility of DINGO-T1 to perform inspiral-merger-ringdown (IMR) consistency tests probing general relativity [4, 70, 71]. For these tests, the

posterior of the final mass M_f and spin χ_f are independently estimated for the inspiral (low) and postinspiral (high frequency) part of the signal, separated by an event-specific cut-off frequency f_{cut} . We perform IMR consistency tests on seven events from O3—with all analyses carried out using the same DINGO-T1 model. We display the fractional deviations between the inspiral and postinspiral parameters in Fig. 3b and find that our analyses show overall consistency with general relativity.

Conclusions.—We introduced DINGO-T1, a transformer-based model that enables fast and flexible GW parameter inference across varying data analysis settings, including detector configurations and frequency ranges. We validated DINGO-T1 on an array of simulated and real data sets, including a realistic catalog analysis involving 17 data configurations. We argued that DINGO-T1 can be used to probe systematics, and demonstrated it can be applied for IMR consistency tests. Thanks to improved architecture and training, we obtain increased median sample efficiency on O3 HL events of 4.2%, compared to 1.4% for a NPE baseline. As we do not leverage knowledge of time-translation equivariances in DINGO-T1, the efficiencies do not fully reach GNPE-level performance. However, DINGO-T1 has greatly increased flexibility and maintains access to the density, making it significantly more useful in practice and enabling further scaling and fine-tuning studies.

A natural next step would be to consider variations

in signal duration by conditioning tokens on frequency resolution information. Another promising direction is to explore alternative data representations such as time domain or time-frequency domain [72] (employing vision transformers [73]), where simpler signal morphology may lead to improved training. In the context of LISA, our approach offers a natural solution to the problem of expected data gaps [31]. In general, the proposed transformer framework and training strategy can be readily extended and adapted to other tasks like signal detection and the DINGO-T1 transformer encoder could serve as a general-purpose GW compression backbone. By concentrating on adaptable models that can be shared across tasks, computational effort can thereby be invested where it most benefits scaling and performance.

Acknowledgments.—We thank Michael Pürrer and Vincent Berenz for helpful discussions, and Ik Siong Heng for comments on the manuscript. A.K. thanks the International Max Planck Research School for Intelligent Systems (IMPRS-IS) for support. S.R.G. is supported by a UKRI Future Leaders Fellowship (grant number MR/Y018060/1). A.B.’s research is supported in part by the European Research Council (ERC) Horizon Synergy Grant “Making Sense of the Unexpected in the Gravitational-Wave Sky” grant agreement no. GWSky-101167314. The computational work for this Letter was performed on the Atlas cluster at the Max Planck Institute for Intelligent Systems. This research has made use of data or software obtained from the Gravitational Wave Open Science Center (gwosc.org), a service of the LIGO Scientific Collaboration, the Virgo Collaboration, and KAGRA. This material is based upon work supported by NSF’s LIGO Laboratory which is a major facility fully funded by the National Science Foundation, as well as the Science and Technology Facilities Council (STFC) of the United Kingdom, the Max-Planck-Society (MPS), and the State of Niedersachsen/Germany for support of the construction of Advanced LIGO and construction and operation of the GEO600 detector. Additional support for Advanced LIGO was provided by the Australian Research Council. Virgo is funded through the European Gravitational Observatory (EGO), by the French Centre National de Recherche Scientifique (CNRS), the Italian Istituto Nazionale di Fisica Nucleare (INFN) and the Dutch Nikhef, with contributions by institutions from Belgium, Germany, Greece, Hungary, Ireland, Japan, Monaco, Poland, Portugal, Spain. KAGRA is supported by Ministry of Education, Culture, Sports, Science and Technology (MEXT), Japan Society for the Promotion of Science (JSPS) in Japan; National Research Foundation (NRF) and Ministry of Science and ICT (MSIT) in Korea; Academia Sinica (AS) and National Science and Technology Council (NSTC) in Taiwan.

* annalena.kofler@tuebingen.mpg.de

- [1] B. P. Abbott *et al.* (LIGO Scientific, Virgo, Fermi GBM, INTEGRAL, IceCube, AstroSat Cadmium Zinc Telluride Imager Team, IPN, Insight-Hxmt, ANTARES, Swift, AGILE Team, 1M2H Team, Dark Energy Camera GW-EM, DES, DLT40, GRAWITA, Fermi-LAT, ATCA, ASKAP, Las Cumbres Observatory Group, OzGrav, DWF (Deeper Wider Faster Program), AST3, CAASTRO, VINROUGE, MASTER, J-GEM, GROWTH, JAGWAR, CaltechNRAO, TTU-NRAO, NuSTAR, Pan-STARRS, MAXI Team, TZAC Consortium, KU, Nordic Optical Telescope, ePESSTO, GROND, Texas Tech University, SALT Group, TOROS, BOOTES, MWA, CALET, IKI-GW Follow-up, H.E.S.S., LOFAR, LWA, HAWC, Pierre Auger, ALMA, Euro VLBI Team, Pi of Sky, Chandra Team at McGill University, DFN, ATLAS Telescopes, High Time Resolution Universe Survey, RIMAS, RATIR, SKA South Africa/MeerKAT), Multi-messenger Observations of a Binary Neutron Star Merger, *Astrophys. J. Lett.* **848**, L12 (2017), [arXiv:1710.05833](https://arxiv.org/abs/1710.05833).
- [2] B. P. Abbott *et al.* (The LIGO Scientific Collaboration and the Virgo Collaboration), Gw170817: Measurements of neutron star radii and equation of state, *Phys. Rev. Lett.* **121**, 161101 (2018).
- [3] R. Abbott *et al.* (LIGO Scientific Collaboration, Virgo Collaboration, and KAGRA Collaboration), Population of merging compact binaries inferred using gravitational waves through GWTC-3, *Phys. Rev. X* **13**, 011048 (2023).
- [4] R. Abbott *et al.* (The LIGO Scientific Collaboration, the Virgo Collaboration, and the KAGRA Collaboration), Tests of general relativity with gwtc-3, *Phys. Rev. D* **112**, 084080 (2025).
- [5] R. Abbott *et al.* (LIGO Scientific Collaboration, Virgo Collaboration, and KAGRA Collaboration), Constraints on the cosmic expansion history from gwtc-3, *The Astrophysical Journal* **949**, 76 (2023).
- [6] A. G. Abac *et al.* (The LIGO Scientific Collaboration, the Virgo Collaboration, and the KAGRA Collaboration), *Gwtc-4.0: Population properties of merging compact binaries* (2025), [arXiv:2508.18083 \[astro-ph.HE\]](https://arxiv.org/abs/2508.18083).
- [7] The LIGO Scientific Collaboration, the Virgo Collaboration, and the KAGRA Collaboration, *Black hole spectroscopy and tests of general relativity with GW250114* (2025), [arXiv:2509.08099 \[gr-qc\]](https://arxiv.org/abs/2509.08099).
- [8] The LIGO Scientific Collaboration, the Virgo Collaboration, and the KAGRA Collaboration, *Gwtc-4.0: Constraints on the cosmic expansion rate and modified gravitational-wave propagation* (2025), [arXiv:2509.04348 \[astro-ph.CO\]](https://arxiv.org/abs/2509.04348).
- [9] G. Ashton *et al.*, BILBY: A user-friendly Bayesian inference library for gravitational-wave astronomy, *Astrophys. J. Suppl.* **241**, 27 (2019), [arXiv:1811.02042 \[astro-ph.IM\]](https://arxiv.org/abs/1811.02042).
- [10] G. Ashton and C. Talbot, Bilby-MCMC: an MCMC sampler for gravitational-wave inference, *Mon. Not. Roy. Astron. Soc.* **507**, 2037 (2021), [arXiv:2106.08730](https://arxiv.org/abs/2106.08730).
- [11] T. D. Gebhard, N. Kilbertus, I. Harry, and B. Schölkopf, Convolutional neural networks: A magic bullet for gravitational-wave detection?, *Phys. Rev. D* **100**, 063015 (2019).
- [12] E. Marx *et al.*, Machine-learning pipeline for real-time detection of gravitational waves from compact bi-

nary coalescences, *Phys. Rev. D* **111**, 042010 (2025), arXiv:2403.18661 [gr-qc].

[13] A. E. Koloniari, E. C. Koursoumpa, P. Nousi, P. Lampropoulos, N. Passalis, A. Tefas, and N. Stergioulas, New gravitational wave discoveries enabled by machine learning, *Mach. Learn. Sci. Tech.* **6**, 015054 (2025), arXiv:2407.07820 [gr-qc].

[14] M. Razzano and E. Cuoco, Image-based deep learning for classification of noise transients in gravitational wave detectors, *Class. Quant. Grav.* **35**, 095016 (2018), arXiv:1803.09933 [gr-qc].

[15] C. Chatterjee, M. Kovalam, L. Wen, D. Beveridge, F. Diakogiannis, and K. Vinsen, Rapid Localization of Gravitational Wave Sources from Compact Binary Coalescences Using Deep Learning, *Astrophys. J.* **959**, 42 (2023), arXiv:2207.14522 [gr-qc].

[16] C. Chatterjee and L. Wen, Premerger Sky Localization of Gravitational Waves from Binary Neutron Star Mergers Using Deep Learning, *Astrophys. J.* **959**, 76 (2023), arXiv:2301.03558 [astro-ph.HE].

[17] H. Gabbard, C. Messenger, I. S. Heng, F. Tonolini, and R. Murray-Smith, Bayesian parameter estimation using conditional variational autoencoders for gravitational-wave astronomy, *Nature Phys.* **18**, 112 (2022), arXiv:1909.06296 [astro-ph.IM].

[18] A. J. K. Chua and M. Vallisneri, Learning Bayesian posteriors with neural networks for gravitational-wave inference, *Phys. Rev. Lett.* **124**, 041102 (2020), arXiv:1909.05966 [gr-qc].

[19] S. R. Green, C. Simpson, and J. Gair, Gravitational-wave parameter estimation with autoregressive neural network flows, *Phys. Rev. D* **102**, 104057 (2020), arXiv:2002.07656 [astro-ph.IM].

[20] S. R. Green and J. Gair, Complete parameter inference for GW150914 using deep learning, *Mach. Learn. Sci. Tech.* **2**, 03LT01 (2021), arXiv:2008.03312 [astro-ph.IM].

[21] A. Delaunoy, A. Wehenkel, T. Hinderer, S. Nissanke, C. Weniger, A. R. Williamson, and G. Louppe, Lightning-Fast Gravitational Wave Parameter Inference through Neural Amortization, in *Third Workshop on Machine Learning and the Physical Sciences* (2020) arXiv:2010.12931 [astro-ph.IM].

[22] M. Dax, S. R. Green, J. Gair, J. H. Macke, A. Buonanno, and B. Schölkopf, Real-Time Gravitational Wave Science with Neural Posterior Estimation, *Phys. Rev. Lett.* **127**, 241103 (2021), arXiv:2106.12594 [gr-qc].

[23] M. Dax *et al.*, Neural Importance Sampling for Rapid and Reliable Gravitational-Wave Inference, *Phys. Rev. Lett.* **130**, 171403 (2023), arXiv:2210.05686 [gr-qc].

[24] U. Bhardwaj, J. Alvey, B. K. Miller, S. Nissanke, and C. Weniger, Sequential simulation-based inference for gravitational wave signals, *Phys. Rev. D* **108**, 042004 (2023), arXiv:2304.02035 [gr-qc].

[25] D. Chatterjee *et al.*, Rapid likelihood free inference of compact binary coalescences using accelerated hardware, *Mach. Learn. Sci. Tech.* **5**, 045030 (2024), arXiv:2407.19048 [gr-qc].

[26] M. Dax *et al.*, Real-time inference for binary neutron star mergers using machine learning, *Nature* **639**, 49 (2025), arXiv:2407.09602 [gr-qc].

[27] W. van Straalen, A. Kolmus, J. Janquart, and C. Van Den Broeck, Pre-Merger Detection and Characterization of Inspiring Binary Neutron Stars Derived from Neural Posterior Estimation, (2024), arXiv:2407.10263 [gr-qc].

[28] K. Cranmer, J. Brehmer, and G. Louppe, The frontier of simulation-based inference, *Proceedings of the National Academy of Sciences* **117**, 30055 (2020).

[29] The LIGO Scientific Collaboration, the Virgo Collaboration, R. Abbott, *et al.*, Gwtc-2.1: Deep extended catalog of compact binary coalescences observed by ligo and virgo during the first half of the third observing run, *Physical Review D* **109**, 022001 (2024).

[30] The LIGO Scientific Collaboration, the Virgo Collaboration, the KAGRA Collaboration, R. Abbott, *et al.*, GWTC-3: Compact Binary Coalescences Observed by LIGO and Virgo During the Second Part of the Third Observing Run, *Physical Review X* **13**, 041039 (2023).

[31] O. Burke, S. Marsat, J. R. Gair, and M. L. Katz, Addressing data gaps and assessing noise mismodeling in LISA, *Phys. Rev. D* **111**, 124053 (2025), arXiv:2502.17426 [gr-qc].

[32] A. Vaswani *et al.*, Attention is all you need, in *Advances in Neural Information Processing Systems*, Vol. 30, edited by I. Guyon *et al.* (Curran Associates, Inc., 2017).

[33] L. Jiang and Y. Luo, Convolutional transformer for fast and accurate gravitational wave detection, in *2022 26th International Conference on Pattern Recognition (ICPR)* (2022) pp. 46–53.

[34] R. Shi, Y. Zhou, T. Zhao, Z. Cao, and Z. Ren, Compact binary systems waveform generation with a generative pretrained transformer, *Phys. Rev. D* **109**, 084017 (2024).

[35] H. Wang, Y. Zhou, Z. Cao, Z. Guo, and Z. Ren, Waveformer: transformer-based denoising method for gravitational-wave data, *Machine Learning: Science and Technology* **5**, 015046 (2024).

[36] C. Chatterjee *et al.*, Pre-trained Audio Transformer as a Foundational AI Tool for Gravitational Waves (2024).

[37] E. Khalouei, C. G. Sabiu, L. M. Hyung, and A. Gopakumar, External attention transformer: A robust ai model for identifying initial eccentricity signatures in binary black hole events in simulated advanced ligo data (2025), arXiv:2506.03634.

[38] P. M. Joshi and R. Prix, Transformer networks for continuous gravitational-wave searches (2025), arXiv:2509.10912 [gr-qc].

[39] L. Papalini, F. D. Santi, M. Razzano, I. S. Heng, and E. Cuoco, Can Transformers help us perform parameter estimation of overlapping signals in gravitational wave detectors? (2025).

[40] S. N. Shukla and B. M. Marlin, A survey on principles, models and methods for learning from irregularly sampled time series (2021), arXiv:2012.00168.

[41] Z. Wang, J. Hasenauer, and Y. Schälte, Missing data in amortized simulation-based neural posterior estimation, *PLOS Computational Biology* **20**, 1 (2024).

[42] M. Gloeckler, M. Deistler, C. D. Weilbach, F. Wood, and J. H. Macke, All-in-one simulation-based inference, in *Proceedings of the 41st International Conference on Machine Learning*, Proceedings of Machine Learning Research, Vol. 235, edited by R. Salakhutdinov *et al.* (PMLR, 2024) pp. 15735–15766.

[43] Y. Verma, A. Bharti, and V. Garg, Robust simulation-based inference under missing data via neural processes, in *The Thirteenth International Conference on Learning Representations* (2025).

[44] J. Aasi *et al.* (The LIGO Scientific Collaboration), Advanced LIGO, *Class. Quant. Grav.* **32**, 074001 (2015), arXiv:1411.4547 [gr-qc].

[45] F. Acernese *et al.* (The Virgo collaboration), Advanced Virgo: a second-generation interferometric gravitational wave detector, *Class. Quant. Grav.* **32**, 024001 (2015), [arXiv:1408.3978 \[gr-qc\]](https://arxiv.org/abs/1408.3978).

[46] T. Akutsu *et al.* (KAGRA), Overview of kagra: Detector design and construction history, *PTEP* **2021**, 05A101 (2021), [arXiv:2005.05574 \[physics.ins-det\]](https://arxiv.org/abs/2005.05574).

[47] The LIGO Scientific Collaboration and the Virgo Collaboration, *GWTC-2.1: Deep Extended Catalog of Compact Binary Coalescences Observed by LIGO and Virgo During the First Half of the Third Observing Run - Parameter Estimation Data Release* (2022).

[48] The LIGO Scientific Collaboration, the Virgo Collaboration, and the KAGRA Collaboration, *Gwtc-3: Compact binary coalescences observed by ligo and virgo during the second part of the third observing run — parameter estimation data release* (2021).

[49] E. Payne, S. Hourihane, J. Golomb, R. Udall, D. Davis, and K. Chatziioannou, Curious case of GW200129: Interplay between spin-precession inference and data-quality issues, *Phys. Rev. D* **106**, 104017 (2022).

[50] R. Udall, S. Hourihane, S. Miller, D. Davis, K. Chatziioannou, M. Isi, and H. Deshong, Antialigned spin of GW191109: Glitch mitigation and its implications, *Phys. Rev. D* **111**, 024046 (2025).

[51] A. Kofler, M. Dax, S. R. Green, J. Wildberger, N. Gupte, J. Macke, J. Gair, A. Buonanno, and B. Schölkopf, *DINGO-T1 model for "flexible gravitational-wave parameter estimation with transformers"* (2025).

[52] C. Talbot, S. Biscoveanu, A. Zimmerman, T. Baka, W. M. Farr, J. Golomb, C. Hoy, A. Lundgren, J. Tissino, M. J. Williams, J. Veitch, and A. Vijaykuma, *Inference with finite time series ii: the window strikes back* (2025), [arXiv:2508.11091 \[gr-qc\]](https://arxiv.org/abs/2508.11091).

[53] G. Papamakarios and I. Murray, Fast ϵ -free inference of simulation models with bayesian conditional density estimation, in *Advances in neural information processing systems* (2016) [arXiv:1605.06376 \[stat.ML\]](https://arxiv.org/abs/1605.06376).

[54] J.-M. Lueckmann, P. J. Gonçalves, G. Bassetto, K. Öcal, M. Nonnenmacher, and J. H. Macke, Flexible statistical inference for mechanistic models of neural dynamics, in *Proceedings of the 31st International Conference on Neural Information Processing Systems* (2017) pp. 1289–1299.

[55] D. Greenberg, M. Nonnenmacher, and J. Macke, Automatic posterior transformation for likelihood-free inference, in *International Conference on Machine Learning* (PMLR, 2019) pp. 2404–2414.

[56] B. P. Abbott *et al.* (The LIGO Scientific Collaboration and the Virgo Collaboration), A guide to LIGO–Virgo detector noise and extraction of transient gravitational-wave signals, *Class. Quant. Grav.* **37**, 055002 (2020), [arXiv:1908.11170 \[gr-qc\]](https://arxiv.org/abs/1908.11170).

[57] S. Vinciguerra, J. Veitch, and I. Mandel, Accelerating gravitational wave parameter estimation with multi-band template interpolation, *Class. Quant. Grav.* **34**, 115006 (2017), [arXiv:1703.02062 \[gr-qc\]](https://arxiv.org/abs/1703.02062).

[58] S. Morisaki, Accelerating parameter estimation of gravitational waves from compact binary coalescence using adaptive frequency resolutions, *Phys. Rev. D* **104**, 044062 (2021), [arXiv:2104.07813 \[gr-qc\]](https://arxiv.org/abs/2104.07813).

[59] Y. N. Dauphin, A. Fan, M. Auli, and D. Grangier, Language modeling with gated convolutional networks, in *Proceedings of the 34th International Conference on Machine Learning - Volume 70*, ICML’17 (JMLR, 2017) p. 933–941.

[60] J. Devlin, M.-W. Chang, K. Lee, and K. Toutanova, BERT: Pre-training of deep bidirectional transformers for language understanding, in *Proceedings of the 2019 Conference of the North American Chapter of the Association for Computational Linguistics: Human Language Technologies, Volume 1 (Long and Short Papers)*, edited by J. Burstein, C. Doran, and T. Solorio (Association for Computational Linguistics, 2019) pp. 4171–4186.

[61] T. Darcet, M. Oquab, J. Mairal, and P. Bojanowski, Vision transformers need registers, in *The Twelfth International Conference on Learning Representations* (2024).

[62] Q. Wang *et al.*, Learning deep transformer models for machine translation, in *Proceedings of the 57th Annual Meeting of the Association for Computational Linguistics*, edited by A. Korhonen, D. Traum, and L. Márquez (Association for Computational Linguistics, 2019) pp. 1810–1822.

[63] R. Xiong *et al.*, On layer normalization in the transformer architecture, in *Proceedings of the 37th International Conference on Machine Learning*, Proceedings of Machine Learning Research, Vol. 119, edited by H. D. III and A. Singh (PMLR, 2020) pp. 10524–10533.

[64] C. Durkan, A. Bekasov, I. Murray, and G. Papamakarios, Neural spline flows, in *Advances in Neural Information Processing Systems*, Vol. 32, edited by H. Wallach *et al.* (Curran Associates, Inc., 2019).

[65] B. Cheng, I. Misra, A. G. Schwing, A. Kirillov, and R. Girdhar, Masked-attention mask transformer for universal image segmentation, in *2022 IEEE/CVF Conference on Computer Vision and Pattern Recognition (CVPR)* (2022) pp. 1280–1289.

[66] G. Pratten *et al.*, Computationally efficient models for the dominant and subdominant harmonic modes of precessing binary black holes, *Phys. Rev. D* **103**, 104056 (2021).

[67] I. Loshchilov and F. Hutter, Decoupled weight decay regularization, in *International Conference on Learning Representations* (2019).

[68] P. Micikevicius *et al.*, Mixed precision training, in *International Conference on Learning Representations* (2018).

[69] M. Dax, S. R. Green, J. Gair, M. Deistler, B. Schölkopf, and J. H. Macke, Group equivariant neural posterior estimation, in *International Conference on Learning Representations* (2022) [arXiv:2111.13139 \[cs.LG\]](https://arxiv.org/abs/2111.13139).

[70] A. Ghosh, N. K. Johnson-McDaniel, A. Ghosh, C. K. Mishra, P. Ajith, W. D. Pozzo, C. P. L. Berry, A. B. Nielsen, and L. London, Testing general relativity using gravitational wave signals from the inspiral, merger and ringdown of binary black holes, *Classical and Quantum Gravity* **35**, 014002 (2017).

[71] R. Abbott *et al.* (LIGO Scientific, Virgo), Tests of general relativity with binary black holes from the second LIGO–Virgo gravitational-wave transient catalog, *Phys. Rev. D* **103**, 122002 (2021), [arXiv:2010.14529 \[gr-qc\]](https://arxiv.org/abs/2010.14529).

[72] N. J. Cornish, Time-Frequency Analysis of Gravitational Wave Data, *Phys. Rev. D* **102**, 124038 (2020), [arXiv:2009.00043 \[gr-qc\]](https://arxiv.org/abs/2009.00043).

[73] A. Dosovitskiy *et al.*, An image is worth 16x16 words: Transformers for image recognition at scale, in *International Conference on Learning Representations* (2021).

[74] N. J. Cornish and T. B. Littenberg, BayesWave: Bayesian Inference for Gravitational Wave Bursts and Instrument Glitches, *Class. Quant. Grav.* **32**, 135012 (2015), [arXiv:1410.3835 \[gr-qc\]](https://arxiv.org/abs/1410.3835).

- [75] T. B. Littenberg and N. J. Cornish, Bayesian inference for spectral estimation of gravitational wave detector noise, *Phys. Rev. D* **91**, 084034 (2015), [arXiv:1410.3852 \[gr-qc\]](https://arxiv.org/abs/1410.3852).
- [76] N. J. Cornish, T. B. Littenberg, B. Bécsy, K. Chatzioanou, J. A. Clark, S. Ghonge, and M. Millhouse, BayesWave analysis pipeline in the era of gravitational wave observations, *Phys. Rev. D* **103**, 044006 (2021), [arXiv:2011.09494 \[gr-qc\]](https://arxiv.org/abs/2011.09494).

Supplemental Material

FULL AMORTIZATION IN GRAVITATIONAL WAVE POSTERIOR ESTIMATION

In gravitational wave (GW) inference, the data representation depends on the analysis settings, such as available detectors and frequency ranges. We define full amortization in this context as the ability to perform parameter estimation with a single model that generalizes across these settings. DINGO-T1 advances toward this goal by learning a flexible representation that adapts to varying data configurations at inference time.

Formally, the goal of GW inference is to estimate the Bayesian posterior over parameters θ

$$p(\theta|d) = \frac{p(\theta)p(d|\theta)}{p(d)} , \quad (2)$$

defined by prior $p(\theta)$ and likelihood $p(d|\theta)$. Assuming additive, stationary, and Gaussian detector noise characterized by its noise amplitude—the power spectral density (PSD) $S_n(f)$ —the likelihood takes the form

$$p(d|\theta, S_n) \propto \exp\left(-\frac{1}{2}(d - h(\theta)|d - h(\theta))_{S_n}\right) , \quad (3)$$

where $h(\theta)$ denotes the simulated GW signal for source parameters θ . With both d and $h(\theta)$ represented as frequency series, the noise-weighted inner product is given by

$$(a|b)_{S_n} = 4 \sum_I \mathcal{R} \int_{f_{\min,I}}^{f_{\max,I}} \frac{a_I^*(f)b_I(f)}{S_{n,I}(f)} df . \quad (4)$$

This inner product—and consequently the likelihood—quantifies how well the simulated signal $h(\theta)$ matches the observed data d across detectors I . Although the posterior $p(\theta|d)$ is often written as depending only on d , it in fact reflects several modeling and analysis choices implicit in Eqs. (2)–(4): the prior distribution, the waveform model used to generate $h(\theta)$, the noise PSDs, the set of detectors, the frequency range $[f_{\min,I}, f_{\max,I}]$, and the discretization Δf defining the resolution of the integral in the inner product. These quantities can vary between events, meaning that a fully amortized inference model $q(\theta|d)$ must accommodate such variations. The DINGO framework already supports changing PSDs via PSD-conditional models $q(\theta|d, S_n)$ [22], and can, in restricted cases, also accommodate varying priors [26]. Adjustments to the lower frequency cutoff $f_{\min,I}$ have been explored by masking the corresponding data segments with zeros [26], though this approach can lead to suboptimal performance and biases in the posterior estimates [41, 43].

A flexible model like DINGO-T1 provides the key to achieving full amortization in GW inference since such a

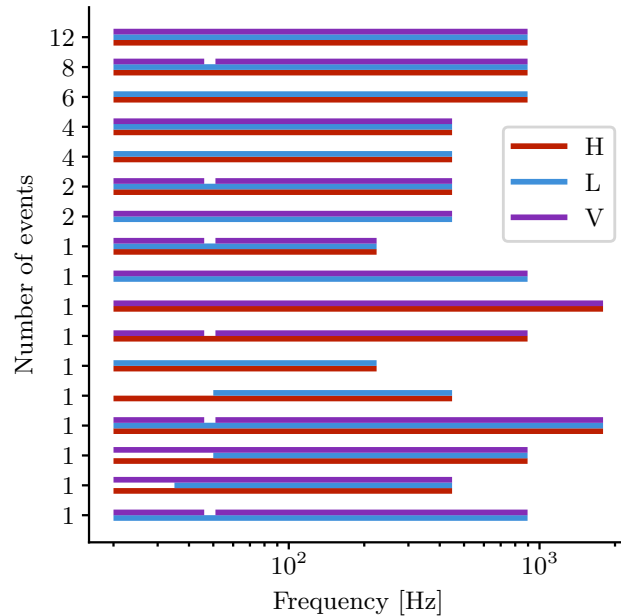


Figure 4. The 48 GW events considered in this study are analyzed in 17 different data analysis settings in O3 LVK catalogs [29, 30]. Each event is based on data from a subset of the three detectors (HLV) and spans frequency ranges that vary with data quality and source properties. The DINGO-T1 model accommodates all of these settings with a single neural network.

model can flexibly accommodate the diverse data analysis settings encountered in practice, as illustrated in Fig. 4 for O3 events. The detector configuration can change from event to event due to maintenance, instrumental issues, earthquakes, or poor data quality [29, 30]. Similarly, the analysis frequency range may be adjusted: the minimum frequency, typically $f_{\min} = 20$ Hz, can be increased to exclude non-Gaussian noise artifacts that cannot be subtracted from the data [29], as is the case for the three events highlighted in Tab. IV. The maximum frequency of each event is determined by the sampling rate f_s needed to fully resolve the signal, with $f_{\max} \propto f_s/2$ [29, 30]. In addition to such global adjustments, narrow frequency bands may be excluded to correct for systematic calibration errors, a procedure known as “PSD notching.” For example, several O3b events involving the Virgo detector exhibited a narrow-band calibration error between 46 Hz and 51 Hz due to a mis-specification in the calibration models. To mitigate its impact on parameter estimation, this frequency interval is effectively removed in standard samplers by assigning an artificially large noise level [30].

In summary, DINGO-T1 amortizes over key data-analysis variations—noise PSDs, detector setups, frequency ranges, and calibration errors—while full amortization over frequency resolution, priors, and waveform models remains future work.

DATA SETTINGS

Prior.— The prior ranges follow [23], except for the luminosity distance, for which we adopt $d_L \in [0.1, 6]$ Gpc. This choice reflects that we train a single DINGO-T1 model rather than three separate models for different d_L ranges.

Frequency settings.— For the 48 events consistent with the chosen prior ranges, we extracted the frequency ranges from the GWTC-2.1 [47] and GWTC-3 [48] data releases and the detector configurations from the corresponding catalogs [29, 30]. These configurations cover an overall frequency range of [20, 1792] Hz, and all events are analyzed using a fixed signal duration of $T = 8$ s, leaving amortization over different frequency resolutions for future work. A complete summary of the event-specific settings is provided in Tab. IV.

Multibanding.— We employ multibanding [57, 58] to compress GW signals without loss of information before passing them to the DINGO-T1 model. In this approach, neighboring frequency bins are averaged when the signal is approximately constant, resulting in a non-uniform frequency grid with coarser resolution at high frequencies. Following [26], the frequency resolution is typically decreased by a factor of two from one multibanded frequency band to the next, with band boundaries (called "nodes") determined by requiring 32 frequency bins per waveform period. However, this approach of determining the bands is not directly applicable to precessing waveforms such as IMRPhenomXPHM [66], because precession introduces complex behavior between zero-crossings. To address this, we decimate 10^3 whitened waveforms for a range of potential compression factors and compute the difference between each decimated waveform and its high-resolution counterpart. This provides a local quality metric for information loss at each frequency. By constraining the maximally allowed local deviation, we identify the frequency above which a lower resolution can be used. Going from lower to higher frequencies, we group consecutive token segments of fixed size until resolution reduction is permitted, defining the nodes of the multibanded frequency domain. To validate the compression as loss-free, we compute the mismatch between 10^3 decimated waveforms and their interpolated counterparts under extreme conditions (minimal chirp mass and maximal time-shift). We obtain a maximal mismatch of $1.3 \cdot 10^{-3}$, comparable to the lower end of mismatches reported between IMRPhenomXPHM and numerical relativity simulations [66].

The resulting multibanded domain defined on the frequency range [20, 1810] Hz achieves a compression factor of ~ 9 and is used to generate a dataset of $2.5 \cdot 10^7$ waveforms for training. Since the multibanding nodes are defined based on the size of the token segment, we can directly partition the multibanded data into segments of fixed length that serve as tokenizer input. We adopt a

token size of 16: smaller tokens (4 or 8) increase sequence length and training time without yielding noticeable improvements in model performance. Larger token sizes would result in less fine-grained control over frequency ranges at inference time.

ARCHITECTURE

Each low-dimensional segment of 16 multibanded frequency bins is mapped to a token embedding vector of length $d_{\text{model}} = 1024$ by the tokenizer, using fully connected layers together with a 512-dimensional residual block. Conditional inputs—including the segment boundaries $(f^{(k)}, f^{(k+1)})$ and the detector identity I (encoded as a one-hot vector)—are injected within the residual block via a gated linear unit [59]. This is illustrated in Fig. 1 on the left at the example of multibanded data from the Hanford detector. We also experimented with an unconditional tokenizer together with additive positional encodings as in standard language models [32]. However, such encodings are less suitable for continuous, non-uniform quantities like frequency values, and multiple encodings would be needed to incorporate both $(f^{(k)}, f^{(k+1)})$ and I , resulting in a large number of design choices. Over the full frequency range, we obtain 69 tokens per detector. Tokens from all detectors are concatenated together with a learnable, randomly initialized summary token [60, 61], yielding a total of $n = 69 \cdot 3 + 1 = 208$ tokens, each of size d_{model} . These token embeddings, represented as $X \in \mathbb{R}^{n \times d_{\text{model}}}$, serve as the input to the transformer encoder which captures complex correlations between the n tokens via masked self-attention:

$$\text{Attention}(Q, K, V) = \text{softmax} \left(\frac{QK^T}{\sqrt{d_k}} + M \right) V \quad (5)$$

where the mask is defined as $M_{ij} = 0$ for allowed and $M_{ij} = -\infty$ for disallowed positions [32, 65] (see Fig. 1 on the right). The query, key, and value matrices are computed as

$$Q = X \cdot W^Q, \quad K = X \cdot W^K, \quad V = X \cdot W^V \quad (6)$$

with weights $W^K, W^Q, W^V \in \mathbb{R}^{d_{\text{model}} \times d_k}$. To capture multiple representation subspaces, attention is extended to h heads, whose outputs are concatenated and combined with the input X via a residual connection. Each token is passed through a feed-forward layer [32], with pre-layer normalization (LN) applied before both the self-attention and feed-forward blocks [62, 63]. We adopt the pre-LN variant instead of the original post-LN design [32] as it enables stable training without learning rate warm-up. After $N = 8$ transformer layers with $h = 16$ attention heads and feed-forward hidden size 2048, the summary token is extracted and projected to a 128-dimensional context vector using a linear layer. We found that varying

the context size between 56 and 256 dimensions does not significantly affect the training loss, indicating that 128 values suffice for subsequent posterior estimation.

For density estimation, we employ a conditional normalizing flow based on the rational-quadratic spline coupling transform [64], using the same architecture as in [23]. The only difference is that we train a standard NPE network and do not include group equivariances between parameters and data [69]. The conditional normalizing flow architecture is identical for all models.

We compare DINGO-T1 to a standard DINGO NPE model, which uses a residual network similar to [22] and employs layer norm instead of batch norm in the embedding network. The initial layer is seeded with components of a singular value decomposition, but we do not keep the initial embedding layer fixed [22] such that we can utilize the same optimizer and scheduler as the DINGO-T1 models. A summary of model sizes is provided in Tab. I.

Table I. Model sizes of the compared architectures.

Method	Number of parameters		
	Embedding network	Normalizing flow	Total
DINGO Baseline	22 Mio.	92 Mio.	114 Mio.
DINGO-T1	68 Mio.	92 Mio.	160 Mio.

MASKING STRATEGIES DURING TRAINING

To ensure the model can flexibly handle different data-analysis settings at inference time, it must be trained on data that reflect such variability. We therefore adopt a training strategy that mimics changing analysis conditions by removing tokens during training. Specifically, we compare two masking strategies: one uninformed by token relationships (random masking), and one that incorporates data-based structure, such as jointly masking tokens from the same detector (data-based masking), illustrated in Fig. 5.

Random masking.— In the naive masking strategy, 40% of training samples are partially masked. For each masked sample, we draw the number of tokens to remove as $n_{\text{masked}} \sim \mathcal{U}[0, 181]$ where the upper bound allows for single-detector scenarios with additional frequency masking. The token mask m is created by randomly selecting n_{masked} tokens, without assuming any domain knowledge. This strategy thus provides unstructured masks (Fig. 5a), serving as a simple baseline for testing the model’s robustness to missing information.

Data-based masking.— Informed by the structure of GW data, we design a second masking strategy that explicitly captures realistic variations in detector configurations and frequency ranges. This procedure accounts for

(1) missing detectors, (2) changes in the frequency range, and (3) narrow-band frequency removal (“PSD notching”).

(1) To simulate missing detectors, we randomly decide whether to mask none (60%), one (30%), or two (10%) detectors. Among the available detectors (H/L/V), the probabilities of masking are 30%, 30%, and 40%, respectively, reflecting Virgo’s larger downtime relative to the LIGO instruments [30]. (2) To model changing frequency ranges, we apply frequency updates to 25% of training samples. For these, we mask the lower part (10%), upper part (70%), or both (20%) of the range, inspired by Fig. 4. Since frequency updates often affect all detectors simultaneously, we apply the same mask across all detectors in 70% of these cases. New cutoff frequencies are drawn from $f_{\min, \text{new}} \sim \mathcal{U}[20, 180]$ Hz and $f_{\max, \text{new}} \sim \mathcal{U}[80, 1810]$ Hz to accommodate frequency updates required for inspiral-merger-ringdown consistency tests. In cases of $f_{\min, \text{new}} > f_{\max, \text{new}}$, we randomly decide to either mask the lower or upper range, depending on the probabilities given above. If a boundary falls within a token, the entire token is masked, ensuring that all affected frequency regions are consistently removed. (3) To emulate PSD notching, we mask a narrow frequency band in 10% of training samples, where the lower bound is sampled uniformly across the frequency range and the width is drawn as $\Delta f_{\text{mask}} \sim \mathcal{U}[0, 10]$ Hz. Overall, this data-based masking procedure closely reflects the detector and frequency conditions encountered in real gravitational-wave analyses, resulting in clearly visible boundaries between tokens from one detector in Fig. 5b. On average, 18.0% of tokens are masked during training for random masking and 25.5% for data-based masking. We experimented with masking percentages ranging from 15% to 30%: Low masking percentages resulted in lower performance in two-detector events, but applying masks to a large number of samples during training can lead to decreased performance in three-detector events.

TRAINING

We train all models using distributed data-parallel multi-GPU training with automatic mixed precision [68] to reduce memory usage. Training is performed on 8 NVIDIA A100-SXM4-80GB GPUs (CUDA 12.1) using the AdamW [67] optimizer ($\beta_1 = 0.8$, $\beta_2 = 0.99$) with a learning rate of 0.001, weight decay of 0.005, and a `ReduceLROnPlateau` scheduler that halves the learning rate when the validation loss stagnates for 10 epochs. To ensure comparability, all models are trained with a fixed batch size of 16,384. Due to memory constraints, the DINGO-T1 models require two gradient accumulation steps per optimizer update, effectively doubling their training time. The total training duration further depends on the scheduler convergence and early-stopping conditions; detailed timings and epoch counts are summarized

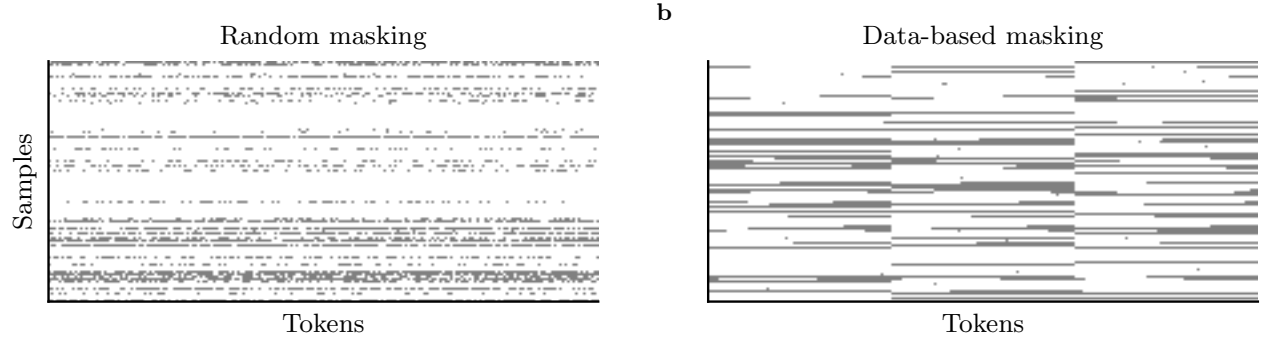


Figure 5. Comparison of (a) random and (b) data-based masking across 100 samples. Data-based masking jointly removes tokens from the same detector, yielding structured patterns, while random masking produces unstructured, scattered masks.

in Tab. II. Because of the long training times, we do not perform extensive hyperparameter optimization beyond a small scan over the initial learning rate, as well as β_1 and β_2 considering the first 50 epochs.

Table II. Training times determined by early stopping.

Method	Epochs	Training time
DINGO Baseline	273	3d 1h
DINGO-T1 Data-based	183	9d 9h
DINGO-T1 Random	219	11d 17h

INFERENCE

During inference, the model has to adapt to the data analysis settings of the event of interest. Since tokens are treated as indivisible elements, any token overlapping a masked range is completely removed, which can lead to slightly larger effective exclusions than strictly necessary. Potential effects on $q(\theta|d)$ are mitigated by performing importance sampling (IS, [23]) in the uniform frequency domain. In IS, importance weights $w_i = p(\theta_i|d, S_n)p(\theta_i)/q(\theta_i|d, S_n)$ are computed for each sample $\theta_i \sim q(\theta_i|d)$. For N weighted samples, the number of effective samples from the posterior $p(\theta|d)$ corresponds to $N_{\text{eff}} = (\sum_{i=1}^N w_i)^2 / (\sum_{i=1}^N w_i^2)$ and we employ the sample efficiency $\epsilon = N_{\text{eff}}/N$ as a performance metric. In practice, a specific number of effective samples is required to obtain a reliable posterior estimate, with $N_{\text{eff}} = 5,000$ defined by the LVK collaboration. Efficiencies $\epsilon \gtrsim 1\%$ therefore indicate that this requirement can be reached with minimal computational cost during IS; higher efficiencies (e.g., 2% vs. 15%) do not substantially reduce runtime and are therefore less critical. For $\epsilon < 1\%$, it is still possible to obtain a sufficient number of effective samples, but at an increased computational cost.

In principle, it is possible to further improve performance of DINGO-T1 by incorporating additional knowl-

edge about equivariances between data and parameters, called *group-equivariant* NPE (GNPE [69]). However, exploiting these equivariances has two main drawbacks: (i) GNPE relies on the convergence of a costly iterative Gibbs sampling procedure at inference time since two models jointly estimate the data standardization and posterior distribution. (ii) GNPE only provides samples from the posterior distribution and the posterior density has to be recovered by training an unconditional normalizing flow to facilitate IS. These points result in a complicated and impractical inference procedure. Furthermore, large inference times of roughly 1 h for 10^5 importance-sampled posterior samples on one NVIDIA-A100 GPU and 64 CPUs [23] limit exploratory interaction when adapting data analysis settings. In contrast, inference times of the DINGO-T1 models are on the order of five to ten minutes for the same number of posterior samples, with initial low-latency samples being available within five seconds. Inference times of DINGO-T1 are dominated by analytically reconstructing the phase ϕ_c which suffers from an inefficient implementation for IMRPhenomXPHM [23].

COMPARING MASKING STRATEGIES

To compare the performance of the two masking strategies, we evaluate both models—trained with either random or data-based masking—on simulated and real events.

Simulated data.—For 1000 simulated signals, we draw 10^5 posterior samples from each DINGO-T1 model across all detector configurations evaluated on the full frequency range and show the obtained sample efficiencies in Fig. 6. While the model trained with random masking achieves median efficiencies of 15.7% (1-detector), 4.9% (2-detector), and 3.4% (3-detector), the efficiencies of the model trained with data-based masking are 26.9%, 6.8%, and 3.3% for one-, two-, and three-detector configurations, respectively. By only changing the detector configuration for each injection, we observe that the model trained with

random masking performs worse on 1- and 2-detector settings. This suggests that randomly masking tokens during training does not translate into performance equivalent to data-based masking. Since we do not apply any frequency masking in this experiment, the random masking seems to have a small advantage on HLV injections. However, the frequency range has to be adapted for observed signals.

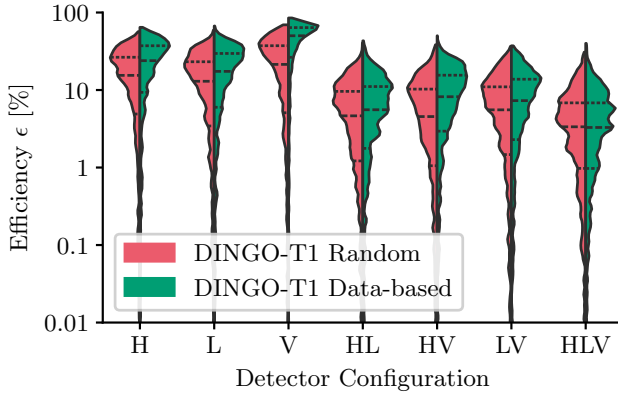


Figure 6. Sample efficiency distributions for 1000 simulated GW signals evaluated with different detector configurations, shown as violin plots. The dashed line represents the median, the dotted lines the quartiles. We compare data-based masking with random token masking for the same DINGO-T1 architecture.

Real events.—We compare the impact of data-based and random masking on observed signals from O3 [29, 30] analyzed with variable data settings (see Fig. 4). We summarize the obtained sample efficiencies in Fig. 7 and provide a detailed event list in Tab. VI. Across the 48 events, we find an overall median efficiency of 2.5% for the model trained with random masking and 4.2% for data-based masking. Specifically, the model trained with random masking obtains 1.2% for 2-detector events (HL: 5.4%, HV: 0.3%, LV: 0.7%), and 2.7% for 3-detector events. DINGO-T1 trained with data-based masking achieves median efficiencies of 4.5% for 2-detector events (HL: 11.0%, HV: 1.1%, LV: 2.2%), and 4.2% for 3-detector events. The baseline DINGO NPE model reaches a median sample efficiency of 1.4% across 30 HLV events evaluated on the full frequency range. In Tab. VI, we observe that sample efficiencies are consistent across models, meaning that a certain event with low efficiency in DINGO-T1 with data-based masking also has similar or even worse performance in the model trained with random masking or in the DINGO NPE baseline. Since data-based masking leads to better results than random masking on real events, we focus on the model with data-based masking in the following and refer to it as the DINGO-T1 model.

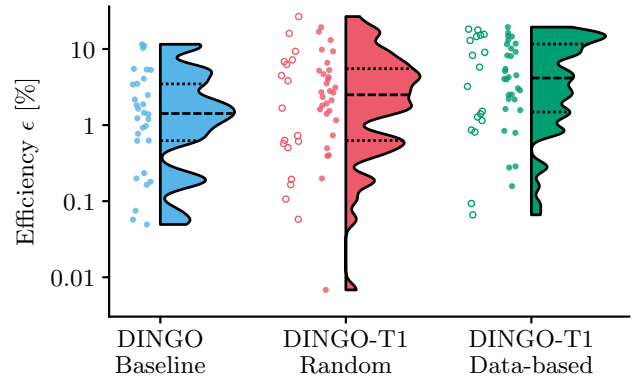


Figure 7. Sample efficiency distributions of DINGO models across the 48 real GW events, shown as violin plots. Dots denote 3-detector events, while circles refer to 2-detector events which cannot be analyzed with the fixed DINGO baseline model. The dashed line represents the median, the dotted lines the quartiles. For the DINGO baseline, we only include the 30 events for which data is available in all three detectors.

VALIDATING DINGO-T1

To ensure that the DINGO-T1 model is well calibrated and aligns with standard methods, we provide P-P plots for each detector configuration and compare posteriors obtained with DINGO-T1 to the standard sampling method Bilby [9], commonly used in official LVK analyses.

P-P plot per detector configuration.—In a P-P plot, the percentile rank of the true value within its posterior marginal is computed, and the cumulative distribution function (CDF) of these ranks is visualized for each parameter. A well-calibrated model yields uniformly distributed percentiles, producing a diagonal CDF. Based on the posterior samples obtained for 10^3 injections, we construct separate P-P plots per detector configuration and include them in Fig. 10. We also report the distribution of p -values from Kolmogorov–Smirnov tests to quantify deviations from uniformity and highlight the parameters where $p < 0.05$, indicating deviations larger than expected under the uniform assumption. Overall, the DINGO-T1 models demonstrate good calibration across all detector configurations on simulated data.

Comparison to Bilby and LVK catalogs.—While we would ideally compare the DINGO-T1 posteriors to the official LVK catalog results, we do not expect perfect agreement between these results due to several reasons: (1) The posterior samples provided by the LVK are obtained using BayesWave PSDs [74–76], while DINGO-T1 is trained with Welch PSDs. Furthermore, we include recent changes regarding the window factor which can lead to biases in the posterior [52]. (2) Posterior samples from the catalogs are mixed results obtained from separate nested sampling runs using different waveform models and reference frequencies. Since we train DINGO-T1 only

on IMRPhenomXPHM, it cannot be guaranteed to obtain aligned posteriors. (3) The prior ranges chosen for DINGO-T1 might not be perfectly consistent with the prior ranges chosen for the analysis of a specific event in the LVK catalogs. To still allow for a valid comparison, we obtain posterior samples with Bilby using the PSDs, waveform model, window factor correction, and prior ranges selected for DINGO-T1. Since it would require significant compute resources to evaluate Bilby on all events reported in this *Letter*, we select GW190701_203306 as an example. In Fig. 8, we show a corner plot of the posterior parameters exhibiting the largest deviations between Bilby and DINGO-T1. To illustrate that a direct comparison to GWTC-2.1 is not possible, we also include the official posterior samples from the LVK data release [47].

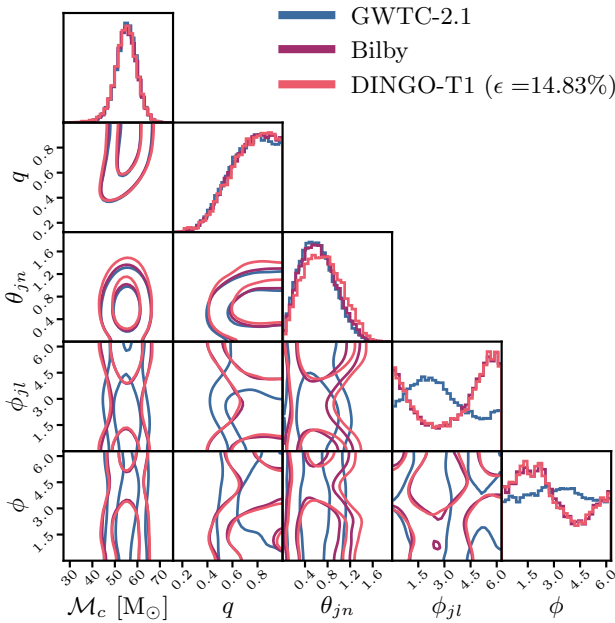


Figure 8. Comparison of DINGO-T1 posteriors to GWTC-2.1 and Bilby results for the event GW190701_203306. Only the parameters displaying the largest deviations between Bilby and DINGO-T1 are included. The GWTC-2.1 posterior displays deviations due to different analysis settings such as the type of PSD, the reference frequency, and mixed posterior samples from different waveform models.

APPLICATIONS

To demonstrate how the flexibility of DINGO-T1 enables new studies and investigations, we select two examples applications:

Posteriors under different detectors.—Since we can flexibly adapt the DINGO-T1 model to a different set of interferometers at inference time, we analyze the 48 events with all possible detector combinations and show the

overview in Tab. VII. The posterior change of an exemplary event is shown in Fig. 3a. Such a study not only shows the consistent performance of DINGO-T1, but it can also provide additional insight into whether certain detectors are responsible for low sample efficiency. For example, GW200129_065458 exhibits low efficiency across all detector configurations involving the Livingston detector—consistent with the glitch subtraction applied in the official LVK analysis. Additionally, low sample efficiency in all detector configurations can point to mistakes in data pre-processing. In an initial analysis of the event GW190517_055101, the Hanford PSD used for conditioning the DINGO models did not capture access power around 500 Hz, resulting in $\epsilon = 0\%$ across all models and detector configurations involving this detector. This failure case is resolved by either masking the affected frequency range or employing a more suitable PSD. The latter leads to an efficiency increase of up to 2.17%.

Inspiral–merger–ringdown consistency tests.—General relativity (GR) can be tested by comparing the final mass and spin of the remnant black hole inferred from the low- and high-frequency parts of the signals [4, 70, 71]. For such inspiral–merger–ringdown (IMR) consistency tests, the frequency-domain signal is divided into two parts defined by the cutoff frequency f_{cut} and both segments—the inspiral part roughly corresponding to $[f_{\text{min}}, f_{\text{cut}}]$ and the postinspiral part corresponding to $[f_{\text{cut}}, f_{\text{max}}]$ —are analyzed separately. The cutoff frequency is defined as the dominant mode GW frequency of a remnant Kerr black hole’s innermost stable circular orbit [4]. To constrain deviations between the inspiral (insp) and postinspiral (postinsp), the following fractional deviations are defined for the final mass M_f and dimensionless spin χ_f :

$$\frac{\Delta M_f}{\bar{M}_f} = 2 \frac{M_f^{\text{insp}} - M_f^{\text{postinsp}}}{M_f^{\text{insp}} + M_f^{\text{postinsp}}} \quad (7)$$

and

$$\frac{\Delta \chi_f}{\bar{\chi}_f} = 2 \frac{\chi_f^{\text{insp}} - \chi_f^{\text{postinsp}}}{\chi_f^{\text{insp}} + \chi_f^{\text{postinsp}}} , \quad (8)$$

where \bar{M}_f and $\bar{\chi}_f$ correspond to the mean of the final mass and spin analyzed with inspiral and postinspiral data. The two dimensional posterior distribution for these fractional deviations is expected to peak at $(0, 0)$ when the test is applied to a signal from a quasi-circular binary black hole coalescence in GR [4, 70, 71].

To demonstrate that we can employ the flexibility of the DINGO-T1 model for in-depth studies, we investigate two separate objectives:

We first perform IMR consistency tests for seven events listed in Tab. III where we analyze the inspiral and postinspiral signals with the DINGO-T1 model and draw 5,000 effective samples for both posteriors. The resulting 2D posterior distributions of fractional deviations are shown in

Table III. Frequency settings for the inspiral-merger-ringdown consistency tests. We provide the colors as a legend for Fig. 3b.

Event	Color	Frequency ranges [Hz]	
		Inspiral	Postinspiral
GW190408_181802	—	[20, 164]	[164, 896]
GW190521_074359	—	[20, 105]	[105, 224]
GW190630_185205	—	[20, 135]	[135, 896]
GW190828_063205	—	[20, 132]	[132, 896]
GW200208_130117	—	[20, 98]	[98, 448]
GW200224_222234	—	[20, 107]	[107, 448]
GW200311_115853	—	[20, 122]	[102, 896]

Fig. 3b which are not reweighed to a uniform prior as in [4] and thus not directly comparable to the results shown in [4].

Second, we repeat the IMR consistency test for GW190630_185205 with different frequency cuts to investigate the robustness of our previous result to varying assumptions about f_{cut} [70]. In addition to $f_{\text{cut}} = 135$ Hz, we choose 120, 130, 140, and 150 Hz and show the results in Fig. 9. While we observe small deviations in the posterior distribution, the result for $f_{\text{cut}} = 135$ Hz is consistent with the results for different frequency cuts.

This flexibility has the potential to reduce the computational cost of IMR consistency tests and facilitate detailed robustness studies.

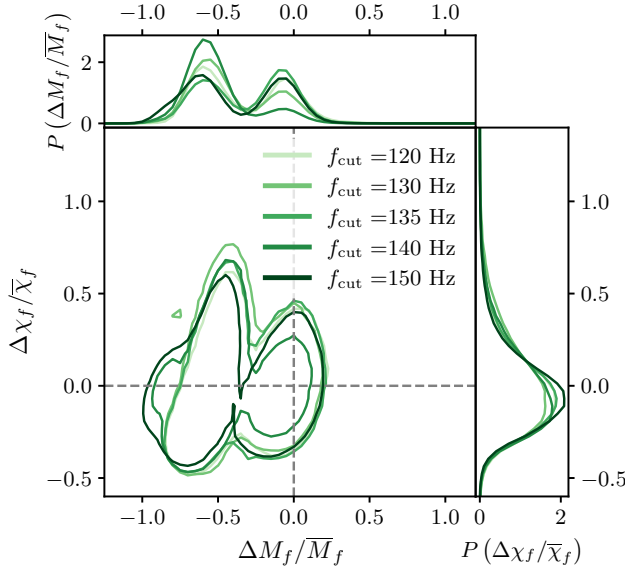


Figure 9. Inspiral-merger-ringdown consistency test for GW190630_185205 where the signal was analyzed with the DINGO-T1 model on the inspiral and postinspiral part of the waveform separated by different f_{cut} values. The main panel shows the 90% credible regions of the 2D posteriors on $(\Delta M_f/\overline{M}_f, \Delta \chi_f/\overline{\chi}_f)$. The side panels show the marginalized posteriors of $\Delta M_f/\overline{M}_f$ and $\Delta \chi_f/\overline{\chi}_f$.

Table IV. Detector and frequency configurations for 48 O3 events. Events with changes to f_{\min} are highlighted in bold. Furthermore, we highlight events where different glitch mitigation techniques were applied to a specific detector: * glitch subtraction, \dagger update of f_{\min} , \diamond BayesWave deglitching, and \ddagger linear subtraction. Details are provided in Table V.

Event	Detectors	f_{\min} [Hz]			f_{\max} [Hz]	PSD Notching (V)		Catalog
		H	L	V		f_{\min} [Hz]	f_{\max} [Hz]	
GW190408_181802	HLV	20	20	20	896	-	-	GWTC-2.1
GW190413_052954	HLV	20	20	20	896	-	-	GWTC-2.1
GW190413_134308*\daggerL	HLV	20	35	20	448	-	-	GWTC-2.1
GW190421_213856	HL	20	20	-	448	-	-	GWTC-2.1
GW190426_190642	HLV	20	20	20	448	-	-	GWTC-2.1
GW190503_185404* L	HLV	20	20	20	896	-	-	GWTC-2.1
GW190513_205428* L	HLV	20	20	20	896	-	-	GWTC-2.1
GW190514_065416*\daggerL	HL	20	50	-	448	-	-	GWTC-2.1
GW190517_055101	HLV	20	20	20	896	-	-	GWTC-2.1
GW190519_153544	HLV	20	20	20	448	-	-	GWTC-2.1
GW190521_074359	HL	20	20	-	224	-	-	GWTC-2.1
GW190527_092055	HL	20	20	-	896	-	-	GWTC-2.1
GW190602_175927	HLV	20	20	20	448	-	-	GWTC-2.1
GW190620_030421	LV	-	20	20	448	-	-	GWTC-2.1
GW190630_185205	LV	-	20	20	896	-	-	GWTC-2.1
GW190701_203306* L	HLV	20	20	20	448	-	-	GWTC-2.1
GW190706_222641	HLV	20	20	20	896	-	-	GWTC-2.1
GW190719_215514	HL	20	20	-	896	-	-	GWTC-2.1
GW190727_060333*\daggerL	HLV	20	50	20	896	-	-	GWTC-2.1
GW190731_140936	HL	20	20	-	896	-	-	GWTC-2.1
GW190803_022701	HLV	20	20	20	896	-	-	GWTC-2.1
GW190828_063405	HLV	20	20	20	896	-	-	GWTC-2.1
GW190910_112807	LV	-	20	20	448	-	-	GWTC-2.1
GW190915_235702	HLV	20	20	20	896	-	-	GWTC-2.1
GW190916_200658	HLV	20	20	20	896	-	-	GWTC-2.1
GW190925_232845	HV	20	-	20	1792	-	-	GWTC-2.1
GW190926_050336	HLV	20	20	20	896	-	-	GWTC-2.1
GW190929_012149	HLV	20	20	20	896	-	-	GWTC-2.1
GW191109_010717 $^{\diamond}$ HL	HL	20	20	-	448	-	-	GWTC-3
GW191127_050227 $^{\diamond}$ H	HLV	20	20	20	896	46	51	GWTC-3
GW191204_110529	HL	20	20	-	896	-	-	GWTC-3
GW191215_223052	HLV	20	20	20	896	46	51	GWTC-3
GW191222_033537	HL	20	20	-	448	-	-	GWTC-3
GW191230_180458	HLV	20	20	20	896	46	51	GWTC-3
GW200112_155838	LV	-	20	20	896	46	51	GWTC-3
GW200128_022011	HL	20	20	-	448	-	-	GWTC-3
GW200129_065458*\ddaggerL	HLV	20	20	20	896	46	51	GWTC-3
GW200208_130117	HLV	20	20	20	448	46	51	GWTC-3
GW200208_222617	HLV	20	20	20	1792	46	51	GWTC-3
GW200209_085452	HLV	20	20	20	896	46	51	GWTC-3
GW200216_220804	HLV	20	20	20	896	46	51	GWTC-3
GW200219_094415	HLV	20	20	20	896	46	51	GWTC-3
GW200220_061928	HLV	20	20	20	224	46	51	GWTC-3
GW200220_124850	HL	20	20	-	896	-	-	GWTC-3
GW200224_222234	HLV	20	20	20	448	46	51	GWTC-3
GW200302_015811	HV	20	-	20	896	46	51	GWTC-3
GW200306_093714	HL	20	20	-	896	-	-	GWTC-3
GW200311_115853	HLV	20	20	20	896	46	51	GWTC-3

Table V. Overview of events from O3 [29, 30] where different glitch mitigation techniques are applied.

Event	Detectors	Mitigation	Affected detectors	Frequency update	Catalog
GW190413_134308* ^{†L}	HLV	glitch subtraction, glitch-only model	L	$f_{\min} = 35$ Hz	GWTC-2.1
GW190503_185404* ^L	HLV	glitch subtraction, glitch-only model	L	-	GWTC-2.1
GW190513_205428* ^L	HLV	glitch subtraction, glitch-only model	L	-	GWTC-2.1
GW190514_065416* ^{†L}	HL	glitch subtraction, glitch-only model	L	$f_{\min} = 50$ Hz	GWTC-2.1
GW190701_203306* ^L	HLV	glitch subtraction, glitch+signal model	L	-	GWTC-2.1
GW190727_060333 ^{†L}	HLV	-	L	$f_{\min} = 50$ Hz	GWTC-2.1
GW191109_010717 ^{◊HL}	HL	BayesWave deglitching	HL	-	GWTC-3
GW191127_050227 ^{◊H}	HLV	BayesWave deglitching	H	-	GWTC-3
GW200129_065458 ^{‡L}	HLV	Linear subtraction	L	-	GWTC-3

Table VI. Sample efficiencies for 48 O3 events with 17 different data analysis settings evaluated with DINGO-T1. The DINGO baseline is evaluated on HLV events without adapting the frequency domain. We highlight events where different glitch mitigation techniques were applied to a specific detector: * glitch subtraction, \dagger update of f_{\min} , \diamond BayesWave deglitching, and \ddagger linear subtraction. Details are provided in Table V.

Event	Det.	DINGO-T1			Event	Det.	DINGO-T1		
		DINGO Baseline	Random	Data-based			DINGO Baseline	Random	Data-based
GW190408_181802	HLV	0.63 %	0.73 %	8.07 %	GW200209_085452	HLV	1.39 %	3.97 %	2.52 %
GW190413_052954	HLV	5.38 %	9.33 %	11.77 %	GW200216_220804	HLV	5.31 %	4.67 %	2.2 %
GW190413_134308* ^{†L}	HLV	1.19 %	5.2 %	4.52 %	GW200219_094415	HLV	4.09 %	3.11 %	5.12 %
GW190426_190642	HLV	0.97 %	0.39 %	0.79 %	GW200220_061928	HLV	0.62 %	1.81 %	10.17 %
GW190503_185404* ^L	HLV	0.18 %	0.5 %	1.57 %	GW200224_222234	HLV	0.23 %	2.67 %	5.49 %
GW190513_205428* ^L	HLV	0.2 %	1.54 %	0.16 %	GW200311_115853	HLV	1.83 %	6.59 %	9.2 %
GW190517_055101	HLV	0.06 %	1.61 %	2.17 %	GW190421_213856	HL	-	9.33 %	17.8 %
GW190519_153544	HLV	1.87 %	1.93 %	4.26 %	GW190514_065416* ^{†L}	HL	-	6.83 %	15.22 %
GW190602_175927	HLV	10.33 %	13.13 %	13.09 %	GW190521_074359	HL	-	0.17 %	1.28 %
GW190701_203306* ^L	HLV	2.17 %	2.81 %	14.83 %	GW190527_092055	HL	-	7.2 %	9.04 %
GW190706_222641	HLV	3.5 %	2.35 %	2.49 %	GW190719_215514	HL	-	6.26 %	14.56 %
GW190727_060333 ^{†L}	HLV	0.77 %	1.41 %	0.84 %	GW190731_140936	HL	-	26.71 %	18.22 %
GW190803_022701	HLV	11.55 %	16.86 %	16.39 %	GW191109_010717 ^{◊HL}	HL	-	0.19 %	1.52 %
GW190828_063405	HLV	0.92 %	4.27 %	3.99 %	GW191204_110529	HL	-	0.11 %	0.07 %
GW190915_235702	HLV	3.42 %	5.29 %	8.23 %	GW191222_033537	HL	-	16.03 %	15.61 %
GW190916_200658	HLV	11.0 %	19.37 %	19.41 %	GW200128_022011	HL	-	4.49 %	8.28 %
GW190926_050336	HLV	1.23 %	3.52 %	1.63 %	GW200220_124850	HL	-	3.83 %	12.94 %
GW190929_012149	HLV	1.64 %	1.16 %	3.04 %	GW200306_093714	HL	-	0.57 %	0.09 %
GW191127_050227 ^{◊H}	HLV	0.16 %	0.4 %	0.28 %	GW190925_232845	HV	-	0.06 %	0.86 %
GW191215_223052	HLV	0.07 %	0.2 %	4.05 %	GW200302_015811	HV	-	0.5 %	1.4 %
GW191230_180458	HLV	5.5 %	9.83 %	14.61 %	GW190620_030421	LV	-	0.63 %	0.81 %
GW200129_065458 ^{‡L}	HLV	0.05 %	0.01 %	0.29 %	GW190630_185205	LV	-	0.61 %	1.15 %
GW200208_130117	HLV	1.46 %	2.12 %	11.58 %	GW190910_112807	LV	-	0.73 %	3.22 %
GW200208_222617	HLV	2.49 %	2.71 %	2.86 %	GW200112_155838	LV	-	1.67 %	5.79 %

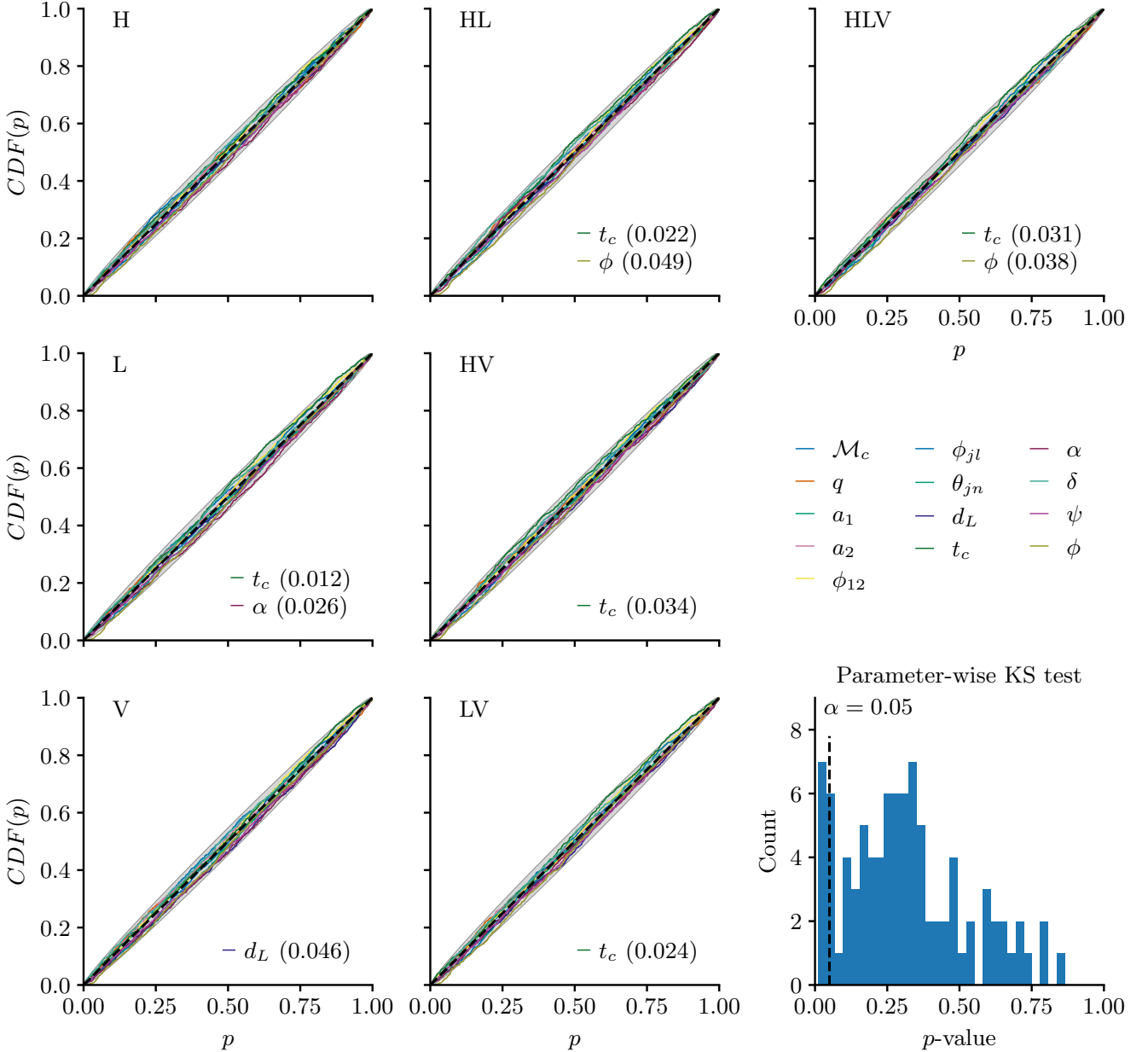


Figure 10. P-P plot for 1000 injections evaluated with different detector configurations for DINGO-T1. The parameters where the Kolmogorov-Smirnov (KS) test falls below $\alpha = 0.05$ are included explicitly and the overall distribution of KS-based p -values is shown in a histogram. We show the 3σ confidence intervals as a gray shaded band.

Table VII. Sample efficiencies for events evaluated on all potential detector configurations with DINGO-T1. We highlight events where different glitch mitigation techniques were applied to a specific detector: * glitch subtraction, \dagger update of f_{\min} , \diamond BayesWave deglitching, and \ddagger linear subtraction. Details are provided in Table V.

Event	Detectors	HLV	HL	HV	LV	H	L	V
GW190408_181802	HLV	8.07 %	8.28 %	0.64 %	1.35 %	2.79 %	6.71 %	62.23 %
GW190413_052954	HLV	11.77 %	9.52 %	2.41 %	0.74 %	9.5 %	18.61 %	37.48 %
GW190413_134308* \dagger L	HLV	4.52 %	7.84 %	8.29 %	1.36 %	21.16 %	11.78 %	32.2 %
GW190426_190642	HLV	0.79 %	2.27 %	7.41 %	0.0 %	29.53 %	0.04 %	49.52 %
GW190503_185404* \dagger L	HLV	1.57 %	1.31 %	1.0 %	0.41 %	17.09 %	2.14 %	60.85 %
GW190513_205428* \dagger L	HLV	0.16 %	0.52 %	4.19 %	2.04 %	11.74 %	4.17 %	22.9 %
GW190517_055101	HLV	2.17 %	4.28 %	1.79 %	0.27 %	1.36 %	0.36 %	13.06 %
GW190519_153544	HLV	4.26 %	0.85 %	3.71 %	4.88 %	3.38 %	9.09 %	59.66 %
GW190602_175927	HLV	13.09 %	13.18 %	28.09 %	5.4 %	27.24 %	15.95 %	26.58 %
GW190701_203306* \dagger L	HLV	14.83 %	14.05 %	9.13 %	5.45 %	31.43 %	5.93 %	38.78 %
GW190706_222641	HLV	2.49 %	5.65 %	13.73 %	6.21 %	0.1 %	10.14 %	27.66 %
GW190727_060333* \dagger L	HLV	0.84 %	17.6 %	2.95 %	3.29 %	5.09 %	0.45 %	23.71 %
GW190803_022701	HLV	16.39 %	28.23 %	19.48 %	9.04 %	28.74 %	7.89 %	42.92 %
GW190828_063405	HLV	3.99 %	17.35 %	8.7 %	7.11 %	24.58 %	9.26 %	64.41 %
GW190915_235702	HLV	8.23 %	13.56 %	0.89 %	5.24 %	1.9 %	14.02 %	42.52 %
GW190916_200658	HLV	19.41 %	20.19 %	5.16 %	18.13 %	11.2 %	27.25 %	42.29 %
GW190926_050336	HLV	1.63 %	4.25 %	11.17 %	12.38 %	16.39 %	19.97 %	53.75 %
GW190929_012149	HLV	3.04 %	4.74 %	10.61 %	0.0 %	24.68 %	0.01 %	50.24 %
GW191127_050227 \diamond H	HLV	0.28 %	0.97 %	8.21 %	5.15 %	16.13 %	28.83 %	6.04 %
GW191215_223052	HLV	4.05 %	5.79 %	5.13 %	1.25 %	6.55 %	2.02 %	56.09 %
GW191230_180458	HLV	14.61 %	8.4 %	2.68 %	16.51 %	7.79 %	16.88 %	58.75 %
GW200129_065458* \dagger L	HLV	0.29 %	0.29 %	2.16 %	0.01 %	14.15 %	0.07 %	2.66 %
GW200208_130117	HLV	11.58 %	12.15 %	5.17 %	5.99 %	32.27 %	8.9 %	17.75 %
GW200208_222617	HLV	2.86 %	2.47 %	4.73 %	0.05 %	5.55 %	18.82 %	18.48 %
GW200209_085452	HLV	2.52 %	11.06 %	3.65 %	16.62 %	9.66 %	34.08 %	41.28 %
GW200216_220804	HLV	2.2 %	12.56 %	12.41 %	7.44 %	21.27 %	10.96 %	52.1 %
GW200219_094415	HLV	5.12 %	7.36 %	3.27 %	2.77 %	11.76 %	11.09 %	1.9 %
GW200220_061928	HLV	10.17 %	18.1 %	6.07 %	7.68 %	8.67 %	11.95 %	61.93 %
GW200224_222234	HLV	5.49 %	7.18 %	1.65 %	6.85 %	10.2 %	20.89 %	4.01 %
GW200311_115853	HLV	9.2 %	5.56 %	11.57 %	4.81 %	7.71 %	4.23 %	3.64 %
GW190421_213856	HL	-	17.8 %	-	-	10.08 %	17.4 %	-
GW190514_065416* \dagger L	HL	-	15.22 %	-	-	19.48 %	4.83 %	-
GW190521_074359	HL	-	1.28 %	-	-	7.24 %	1.26 %	-
GW190527_092055	HL	-	9.04 %	-	-	2.95 %	5.56 %	-
GW190719_215514	HL	-	14.56 %	-	-	17.56 %	0.05 %	-
GW190731_140936	HL	-	18.22 %	-	-	38.6 %	4.69 %	-
GW191109_010717 \diamond HL	HL	-	1.52 %	-	-	0.11 %	5.15 %	-
GW191204_110529	HL	-	0.07 %	-	-	19.49 %	13.28 %	-
GW191222_033537	HL	-	15.61 %	-	-	6.84 %	16.18 %	-
GW200128_022011	HL	-	8.28 %	-	-	38.67 %	18.79 %	-
GW200220_124850	HL	-	12.94 %	-	-	23.86 %	15.56 %	-
GW200306_093714	HL	-	0.09 %	-	-	6.0 %	0.08 %	-
GW190925_232845	HV	-	-	0.86 %	-	8.16 %	-	16.97 %
GW200302_015811	HV	-	-	1.4 %	-	2.25 %	-	31.8 %
GW190620_030421	LV	-	-	-	0.81 %	-	1.5 %	55.53 %
GW190630_185205	LV	-	-	-	1.15 %	-	7.98 %	16.08 %
GW190910_112807	LV	-	-	-	3.22 %	-	4.2 %	19.1 %
GW200112_155838	LV	-	-	-	5.79 %	-	16.7 %	20.93 %